Proceedings of the 4th Jagiellonian Symposium on Advances in Particle Physics and Medicine

Promising Detector Concepts to Advance Coincidence Time Resolution for Time-of-Flight Positron Emission Tomography

C.S. Levin*

Departments of Radiology, Physics, Electrical Engineering, Bioengineering, Stanford University, James H. Clark Center, 318 Campus Drive, Stanford, CA, 94305-5427, U.S.A.

Doi: 10.12693/APhysPolA.142.422 *e-mail: cslevin@stanford.edu

In this paper, we describe design considerations and promising detector technologies for time-of-flight positron emission tomography (TOF-PET). During a positron emission tomography scan, TOF-PET enables positron annihilation events to be positioned closer to their true origin along system response lines, thus facilitating improved reconstructed image signal-to-noise ratio, which has benefits such as better disease visualization and quantification, lower injected dose, and/or lower study duration. The degree of this image signal-to-noise ratio boost is determined by the annihilation photon pair coincidence time resolution of the detector system. Thus, there has been much research and development to advance detector coincidence time resolution, which is the foundation for future TOF-PET system designs. But when considering novel TOF-PET detector designs, it is important to select approaches that enhance coincidence time resolution without a tradeoff of decreasing detection efficiency (e.g., employing thin or low-density detector materials or low intra- or inter-module packing fraction, etc.). One might even argue that high coincidence detection efficiency (a.k.a. *sensitivity*) is the primary goal of any new positron emission tomography system design. In this paper, we will briefly discuss fundamental limitations on positron emission tomography coincidence time resolution using scintillation detectors and describe new detector configurations and electronic readout designs that attempt to address those constraints and achieve as low as 100 ps coincidence time resolution without compromising overall detection efficiency. We also concisely describe an innovative, non-scintillation-based, fast detection concept, which borrows ideas from the field of optics and could, in theory, achieve $\sim$ 1 ps coincidence time resolution. If successful, these technologies will lead to next-generation systems that enhance TOF-PET's ability to visualize and quantify disease.

topics: time-of-flight positron emission tomography (TOF-PET), coincidence time resolution (CTR), scintillation detectors, optical modulations

1. Introduction

When considering potential time-of-flight positron emission tomography (TOF-PET) detector designs with the goal of advancing coincidence time resolution (CTR), it is important to make choices that also preserve the overall coincidence detection efficiency of the system. For example, consider the case where a system designer has a goal to improve CTR by a factor of four over the state-of-the-art commercial PET system design (e.g., from 200 to 50 ps full width at half maximum (FWHM)). This superb CTR enhancement yields a two-fold signal-to-noise ratio (SNR) boost of the reconstructed image based on TOF considerations alone. But if, in order to achieve this excellent CTR, one selects a detector design that employs thin or low Z material and/or a detector design with poor intra- or inter-crystal packing fraction that reduces the overall coincidence detection efficiency by more than a factor of four, the end result would be worse, not better-reconstructed SNR. Example detector design approaches currently under investigation that propose to achieve $\sim$ 100 ps FWHM CTR by employing low Z, low-density materials are described in [1–6].

Figure 1 depicts two example scintillation detector array designs that promote high 511 keV photon detection efficiency while still enabling one to achieve excellent (e.g., $<$ 200 ps FWHM) CTR. The discrete crystal array design (Fig. 1a) has arguably the best detector SNR, and thus better achievable CTR, since the fraction of available scintillation light that results from a 511 keV photon interaction is concentrated onto one or a few silicon photomultipliers (SiPMs) [7]. The monolithic design (Fig. 1b) has a better crystal packing fraction, but since the light is spread onto multiple SiPMs, each with uncorrelated noise contributions, the SiPM array may need to be cooled in order to achieve excellent CTR [8].

For building a TOF-PET system, developing a scalable electronic readout system is also critical. Although many in our field employ digital

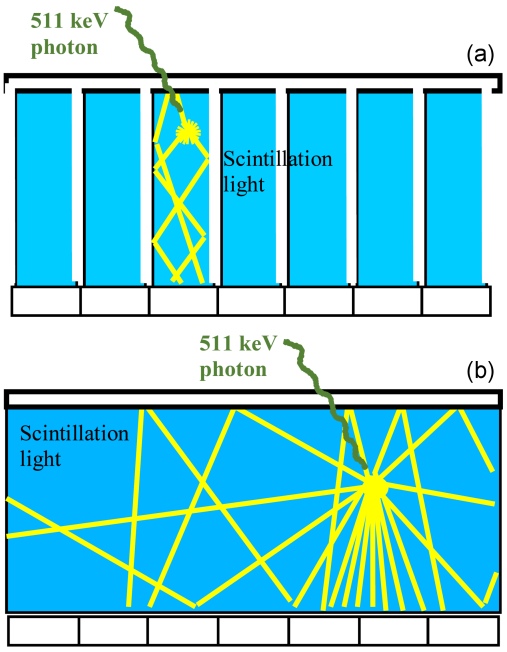

Fig. 1. Examples of PET scintillation detector module configurations that promote high system sensitivity. (a) Discrete crystal design comprising an array of fine rod-shaped elements (blue) optically isolated with a reflector; scintillation light photons (yellow) produced in any crystal as a result of a 511 keV photon (dark green) interaction are focused onto just one or a small number of SiPMs (white) at the bottom. (b) In the monolithic design crystal (blue), scintillation light is spread over several SiPMs.

storage oscilloscope (DSO) for basic detector prototyping studies, more scalable solutions involve dedicated PET integrated circuits (IC) that output digital values representing event time stamp and energy [9], or hybrid designs with a high precision front-end IC, but a separate time-to-digital converter scheme [10, 11].

In this paper, we highlight three high-sensitivity TOF detector design configurations under construction at Stanford University. More details can be found in the cited references. The first, which has demonstrated $\sim$ 230 ps FWHM CTR, is for a TOF-PET insert compatible with magnetic resonance imaging (MRI). The second scheme achieves $\sim$ 100 ps FWHM CTR, and is for a prototype TOF-PET/CT (computed tomography) system. The third detector technology we discuss takes a completely different direction that exploits small perturbations in optical properties (e.g., refractive index or absorption) that result from ionization-induced 511 keV interactions in the material, which can be probed with a laser, with the goal of reaching $<$ 10 ps FWHM CTR. If successful, these three new detector technologies will lead to next-generation TOF-PET systems with enhanced ability to visualize, quantify, and characterize the disease.

2. Materials, methods and results

2.1. Detector design that achieves $\sim$ 230 ps FWHM CTR

Figure 2a shows a picture of the basic detector sub-module for a magnetic resonance (MR)-compatible PET insert for simultaneous PET/MR [9]. The sub-module comprises an 8×16 array of $3.2 \times 3.2 \times 20$ mm^3 lutetium-yttrium oxyorthosilicate (LYSO) scintillator crystals coupled one-to-one (i.e., as per Fig. 1a) to an array of matching SiPM pixels (SensL J-Series), which are read out by a fast timing integrated circuit (PETA6, University of Heidelberg). Six sub-modules arranged on a readout board form a detector module (Fig. 2b). Experiments using 4 pairs of detector modules (6144 LYSO elements total) in coincidence achieve global results of 230.4 ± 0.2 ps FWHM CTR and $11.3 \pm 0.1\%$ FWHM for the 511 keV photopeak energy resolution (ER).

2.2. Detector design that achieves $\sim$ 100 ps FWHM CTR

In order to advance CTR down to $\sim$ 100 ps FWHM while preserving overall detection efficiency, one has to take special care to mitigate additional sources of temporal variations in the detection process, such as variable light collection efficiency and scintillation light transit time to the photodetector, owing to variations in 511 keV photon interaction depth in the long and narrow crystal elements, as well as the effective single photon time resolution (SPTR) of the photodetector, and readout and digitizing electronic noise. In the standard approach (e.g., Fig. 1a, Fig. 2a), the scintillation light resulting from 511 keV photon interactions is collected from the small (e.g., 3×3 mm^2) ends of each rod element in the crystal array (Fig. 3a), which is

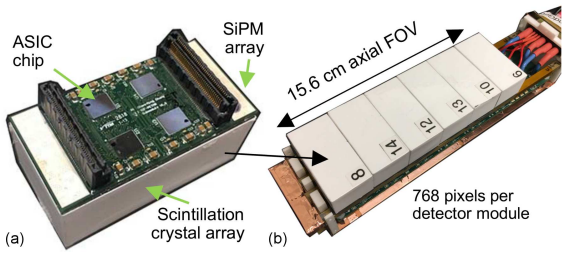

Fig. 2. Scintillation detection module design for an MRI-compatible TOF-PET insert that achieves $\sim$ 230 ps FWHM CTR. (a) Sub-module design comprising an 8×16 array of $3.2 \times 3.2 \times 20$ mm^3 LYSO scintillation crystal elements covered with white reflector coupled end-on to a matching array of 3×3 mm^2 SiPMs read out by PET ICs. (b) Six sub-modules plug into a detector module board that is in contact with a water chilled structure; the entire detector module is housed within a Faraday cage (not shown) for RF shielding.

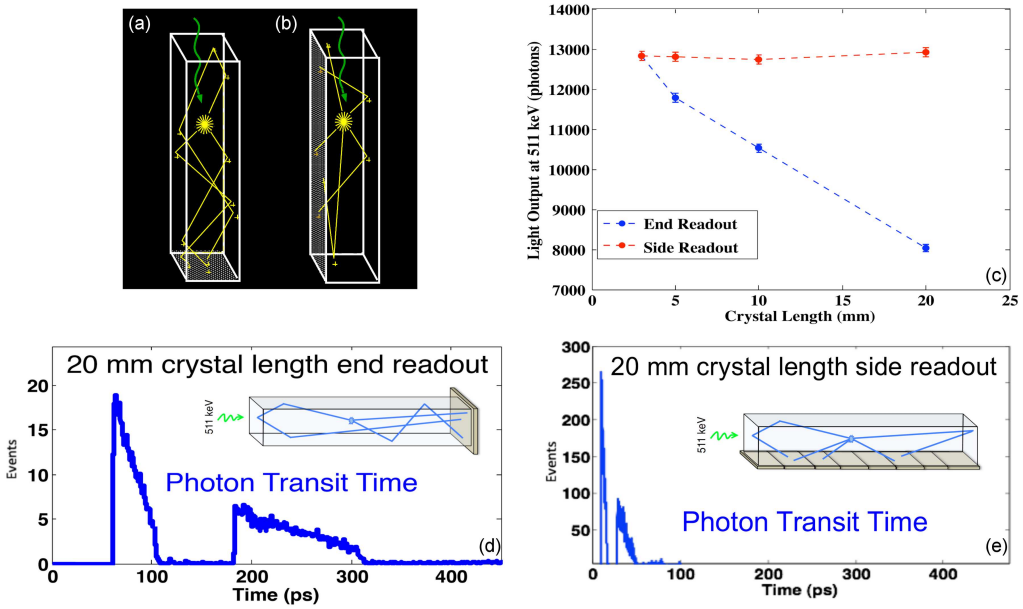

Fig. 3. New scintillation detector configuration that achieves $\sim$ 100 ps FWHM CTR. (a) In the standard configuration, scintillation light created from an ionizing interaction is created somewhere in a rod-shaped crystal element is collected in one or more photodetectors at the small area end (e.g., 3×3 mm^2); (b) in this new scheme, the light is read out from the large area side (e.g., 3×20 mm^2), improving the light collection aspect ratio (c) (experimental data) and reducing the scintillation light transit time spread to the photodetector (e) compared to (d) (simulated data).

a configuration that is subject to significant scintillation light collection efficiency and transit time variations (Fig. 3c (blue line), and Fig. 3d, respectively) [12], depending on the 511 keV photon interaction depth. Figure 3b depicts a novel scintillation detection configuration that enables one to collect more light from crystal elements per interaction with less temporal variation, while preserving high 511 keV photon detection efficiency. In this new arrangement (Fig. 3b), the light is collected from the larger area (e.g., 3×20 mm^2) side faces, which, owing to a much better light collection aspect ratio, has much higher (i.e., $> 90\%$) light collection efficiency (Fig. 3c) [12] and lower scintillation light transit time to the photodetector (Fig. 3e) [12]. Notably, in this side readout configuration, these parameters do not vary significantly with 511 keV photon interaction depth.

Figure 4a shows a proof-of-principle detector module employing this side-readout concept comprising four layers. Each layer comprises a 2×4 array of $3 \times 3 \times 10$ mm^3 LYSO crystal elements, each coupled sideways to linear arrays of 3 mm SiPMs (3 SiPMs per 10 mm crystal element). In this manner, 511 keV photons entering from the left (as shown in the figure) encounter at least 20 mm of LYSO in order to preserve high intrinsic detection efficiency. The timing signals from the 24 SiPMs of each detector layer are multiplexed into one timing channel, so that there are just four timing channels for this four-layer module. We placed a Ge-68 positron source in between two of these four-layer prototype modules and collected coincidence data using a 350–650 keV energy window. The resulting coincidence time spectrum is presented in Fig. 4b, showing a 105 ps FWHM CTR. Obviously, for high crystal packing fraction, it is important that the boards of each detector layer are much thinner than shown in this proof-of-principle configuration. Current efforts involve migrating the board technology to flex circuits with a goal to have a total of $\sim$ 200 μm between the 2×4 crystal arrays of each layer, including the flex circuit, the SiPM thickness, and the top reflector of each 2×4 crystal array. As there also do not exist any PET application-specific integrated circuit (ASIC) chips that are capable of achieving 100 ps CTR, we have developed our own signal processing chain comprising a fast comparator, noise-mitigating circuitry, and field-programmable gate array (FPGA)-based time-to-digital converter (TDC) [10, 11].

2.3. Toward 1 ps CTR: Ionizing radiation detector design based on modulation of optical properties rather than scintillation

Is there a PET detector technology that can achieve $\leq$ 10 ps CTR FWHM? At that timescale, the temporal resolution of conventional scintillation detection is physically limited by the scintillation mechanism itself (as well as the SPTR of the photodetector). However, primary charge carriers that result from an ionizing radiation interaction are created on the femtosecond time scale [13]. How can we access that detection time scale?

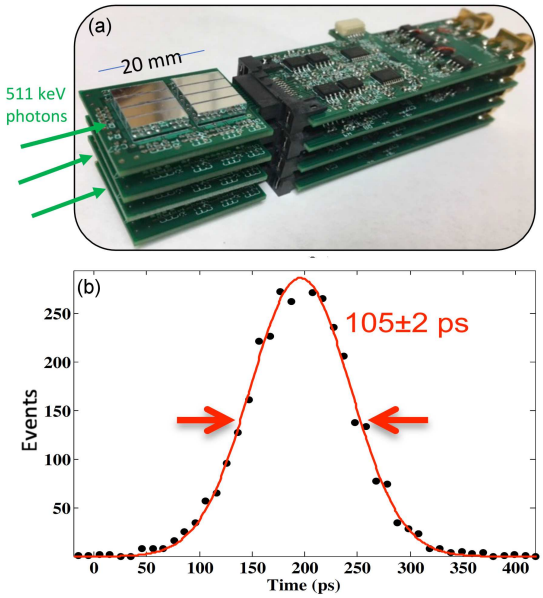

Fig. 4. Proof-of-principle of the side readout scintillation detection concept. (a) Prototype module comprising four layers, each having 2×4 arrays of $3 \times 3 \times 10$ mm^3 LYSO elements side-coupled to linear arrays of SiPMs mounted on printed circuit board (PCB) readout boards, with a total of one multiplexed timing channel per layer. (b) Two such prototype modules in coincidence, with off-board TDCs, achieve $\sim$ 105 ps FWHM CTR. We are currently replacing the relatively thick PCBs housing the SiPMs with thin flex circuits to facilitate high inter-layer crystal packing fraction so that the proposed CTR enhancement is also accompanied by high coincidence detection efficiency, as required for a practical TOF-PET detector.

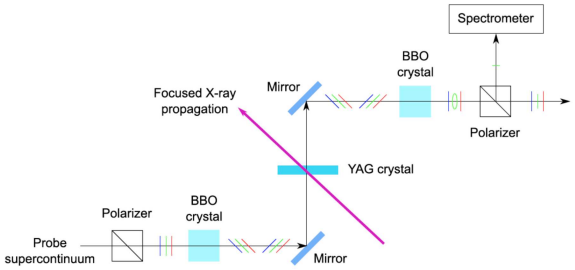

Fig. 5. Schematic optical setup of *interferometric spectral encoding* method that encodes the time of arrival of ionizing interactions into a modulated spectral (wavelength) component of the linearly polarized probe pulses using data collected by a spectrometer to detect the modulated wavelength and map it to arrival time with extremely high temporal precision [13].

Measurements of picosecond and sub-picosecond modulations of optical properties are common in ultrafast optics. Combining these two fields of ionizing radiation detection and ultrafast optics thus seems promising to dramatically improve PET CTR. This leads us to the key question: Can the ionization charge created from a single 511 keV interaction in a material produce a fast change in the optical properties of that material (e.g., refractive index, absorption, etc.) that can be measured with modern optics techniques? We have studied different approaches to answer this question (for example, see [14, 15]), and we believe we have found a promising different approach, which we refer to as *interferometric spectral encoding* [13].

Figure 5 presents a schematic of the interferometric spectral encoding setup we have used to experimentally demonstrate that ionizing photon interactions modulate the optical properties of crystals with *femtosecond scale* temporal resolution [13]. Figure 6 depicts the resulting step-by-step processing of the probe beam. A temporally dispersed white-light pulsed probe source (with the red region of the spectrum arriving a few picoseconds before the blue region) (Fig. 6a) passes through a linear polarizer followed by an alpha barium borate (α-BBO) birefringent crystal that introduces a few picoseconds delay between the vertical and horizontal components of the resulting linear polarization (Fig. 6b). The beam then passes through a yttrium aluminum garnet (YAG) crystal, and then both polarization components transmit through a matched birefringent crystal with a complementary orientation to the first one. This second BBO crystal compensates for the original birefringent delay of the first BBO crystal so that, in the absence of ionizing radiation, the two polarization components phase match in time, and the vertical and horizontal polarizations constructively add to form the original 45° linear polarization for all wavelengths of the probe pulse.

However, when ionizing radiation (X-rays in [13]) interacts in the YAG crystal along the path of the beam, owing to the ionization-induced refractive index modulation, the transmitted probe pulse experiences an induced phase change and small amplitude depletion (see Fig. 6c) at that instant of the interaction. Since the vertical and horizontal polarization components are separated in time, there is an offset in the wavelength location of the phase shift. After the re-time with the second birefringent crystal (Fig. 6d), as a result, a portion of the spectrum is modified by the X-ray interaction for only one of the two polarization components. So, in this case of ionizing interactions in the YAG crystal, the vertical and horizontal components of the polarization constructively add to form the original polarization *except* in the intermediate region that experienced a phase modulation for one of the polarization components but not the other. For these intermediate wavelengths, clean linear 45° polarization is not achieved, and elliptical polarization results. The cross-polarized component (−45°) can then be detected (Fig. 6e). This modulated portion of the spectrum is isolated

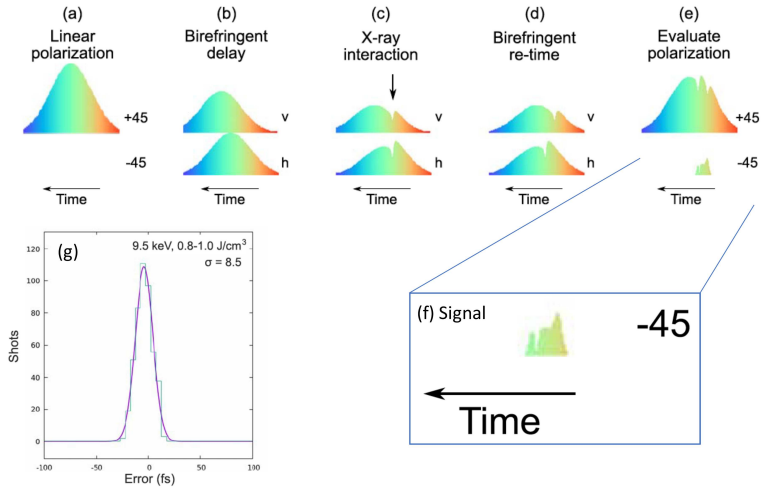

Fig. 6. Illustration of the probe laser spectrum during the interferometric spectral encoding detection process. Probe laser spectra are shown (a) for the original state, (b) after birefringent delay by the first BBO crystal, (c) after X-ray interaction, (d) after birefringent re-timing by the second BBO crystal, (e) at the final evaluation step. +45 and −45 denote the original linear 45° polarization and the cross-polarized component (−45°) respectively. Here, v and h represent the vertical and horizontal polarization components. (f) The signal is the small orthogonal polarization component that is created by the ionization-induced phase modulation. (g) After a calibration step that maps modulated spectral component to ionizing event arrival time, the rising and falling edges of the signal are analyzed, yielding < 10 fs temporal variance for this experimental measurement of ionization-induced modulation of optical properties [13].

by a −45° polarizer and then directed to the entrance slit of a 50 line mm^{-1} grating-based spectrometer (Princeton Instruments) with a high frame rate imaging sensor mounted at the spectrally dispersed image plane of the entrance slit. Thus this is essentially a self-reference interferometer where the two arms are the two polarization components, and the ionization-induced modulation signal is the small cross-polarized component (Fig. 6f).

The term *spectral encoding* is used since the time of arrival information of the ionization event is encoded in the spectral component (the wavelength) of the modulated probe pulse. Systematically varying the delay between the X-ray pulse and the probe continuum pulse allows us to calibrate the monotonic wavelength to ionizing event time mapping [13]. The temporal resolution is obtained by analyzing the rising or falling edge of the small cross-polarized component modulation signal (Fig. 6f). This technique was tested for low-energy X-ray pulses (e.g., 10 keV). By analyzing the rise and fall of this modulation signal, a temporal resolution of < 10 fs σ was achieved (Fig. 6g) [13]. Note that as this approach encodes the fast timing signal from an ionization event into the spectrum of the probe laser, with the signal read out by a spectrometer, this approach obviates the need for fast readout electronics.

Although this spectral encoding method was demonstrated with synchronized low-energy X-ray pulses, we are currently refining this approach to work for the detection of asynchronous individual 511 keV photon interactions. This includes features that greatly enhance sensitivity to lower ionization power deposited in the detection crystal and a revised optical configuration that enables high crystal packing fraction to preserve high detection efficiency.

3. Discussion

We have presented three detector designs with successively improved CTR, from ∼ 200 ps down to ∼ 1 ps, while also preserving high detection efficiency. The first two are scintillation detection technologies, and the third — a new concept based on an interferometric measurement of the modulation of optical properties as a result of an ionizing event.

The detector design employed in the PET insert for MRI utilizes LYSO crystal elements coupled one-to-one to matching SiPM pixels so that scintillation light created from a 511 keV interaction is concentrated onto just one photodetector (Figs. 1a and 2). This design also uses an all-in-one readout IC that outputs digital values representing event timing and energy. If this system is successfully completed, the proposed goal of 230 ps FWHM CTR for this insert system will be among the best CTR performance achieved for TOF-PET/MR imaging.

The goal of ∼ 100 ps FWHM CTR requires us to re-examine sources of temporal variation in the scintillation detection process, including crystal geometry-related light transport effects as well as electronic readout and digitization contributions. To mitigate the effects of interaction-depth

varying scintillation light collection efficiency and transit time to the photodetector, we employ a new configuration where each crystal rod element in an array is read out from its large area side face (Fig. 3b) instead of its small area end (Fig. 3a), in order to achieve higher light collection efficiency (Fig. 3c) and shorter transit time to the photodetector (Fig. 3d, e), independent of crystal length. This arrangement imposes a requirement that the circuit board housing the SiPM arrays for each side-coupled detector layer is extremely thin (e.g., < 200 μm) in order to preserve a high crystal packing fraction. As the available PET readout, ICs cannot yet achieve 100 ps CTR with $3 \times 3 \times 20$ mm^3 crystal elements, we developed our own hybrid readout scheme based on a fast comparator, noise-mitigating circuitry, and FPGA-based TDC. If the $\sim$ 100 ps FWHM CTR result (Fig. 4b) from our proof-of-principle arrangement (Fig. 4a) is successfully scaled to a full system, this will represent the best CTR achieved in a TOF-PET/CT system.

When looking to further improve the CTR down to the $\sim$ 1 ps FWHM range, the intrinsic temporal variations of the scintillation mechanism itself must be considered. One approach is to attempt to probe the earliest step in the ionization radiation detection process: the production of an ionization track, which, as we have shown experimentally, has temporal variance in the femtosecond realm. But it is clear that probing this time scale cannot be accomplished with a scintillation detector, as luminescence occurs several steps after the ionization is first created. Instead, we study the transient modulation of optical properties (refractive index, polarization, and phase) that result from ionizing interaction-produced tracks of electron-hole pairs.

We probed these ionization trajectories with a light pulse whose spectral components arrive at different times and formulated a self-referenced interferometer using the two components of the linearly polarized beam. One of them is delayed with respect to the other and undergoes the ionization-induced modulation at a certain spectral component (wavelength), which is then combined with the other polarization component, giving a small net polarization in the direction orthogonal to the linear polarizer, as measured by a spectrometer (Figs. 5 and 6). In this manner, the precise time of the ionizing interactions is encoded in the particular spectral component that is transiently modulated (Fig. 6). And after a calibration that maps the modulation wavelength component to ionizing interaction time, the rising and falling edges of the modulation signal (the small orthogonal polarization component) (Fig. 6f) are used to demonstrate < 10 fs scale temporal variance (Fig. 6g). Note that since we use a spectrometer to detect the signal and map wavelength to precise timing (Fig. 5), a fast photodetector and fast readout electronics are not needed for this novel detection concept, avoiding those sources of temporal variation.

4. Conclusions

In summary, TOF is the foundation of future PET system designs. If successful, the detection technologies described in this paper, as well as other schemes that improve CTR for TOF-PET performance without compromising detection efficiency, will substantially boost reconstructed image SNR, enhancing PET's ability to characterize the molecular and cellular pathways of disease and guide novel treatments.

Acknowledgments

The research reported in this paper was supported in part by NIH grants R01 EB019465, R01CA214669, R01EB025125, and R01EB023903.

References

[1] P. Lecoq, *Eur. Phys. J. Plus* **137**, 964 (2022).

[2] P. Lecoq G. Konstantinou, R. Latella et al., *IEEE Trans. Radiat. Plasma Med. Sci.* **6**, 510 (2022).

[3] P. Lecoq, C. Morel, J.O. Prior et al., *Phys. Med. Biol.* **65**, 21RM01 (2020).

[4] P. Moskal, O. Rundel, D. Alfs et al., *Phys. Med. Biol.* **61**, 2025 (2016).

[5] P. Moskal, E.L. Stepien, *PET Clin.* **15**, 439 (2020).

[6] P. Moskal, P. Kowalski, R.Y. Shopa et al., *Phys. Med. Biol.* **66**, 175015 (2021).

[7] J.W. Cates, C.S. Levin, *Phys. Med. Biol.* **61**, 2255 (2016).

[8] G. Borghi, Va. Tabacchini, R. Bakker, D.R. Schaart, *Phys. Med. Biol.* **63**, 155006 (2018).

[9] Q. Dong, B.J. Lee, C.-M. Chang, I. Sacco et al., in: *IEEE Nuclear Science Symp. (NSS) and Medical Imaging Conference (MIC), Manchester*, 2019.

[10] S. Pourashraf, A. Gonzalez-Montoro, J.Y. Won, M.S. Lee, J.W. Cates, Z. Zhao, J.S. Lee, C.S. Levin, *Phys. Med. Biol.* **66**, 085005 (2021).

[11] S. Pourashraf, A. Gonzalez-Montoro, M.S. Lee, J.W. Cates, J.Y. Won, J.S. Lee, C.S. Levin, *IEEE Trans. Rad. Plasma Med. Sci.* **6**, 690 (2022).

[12] J.W. Cates, C.S. Levin *Phys. Med. Biol.* **63** 115011 (2018).

[13] L. Tao, R.N. Coffee, D. Jeong, C.S. Levin, *Phys. Med. Biol.* **66**, 045032 (2021).

[14] L. Tao, L. Tao, H.M. Daghighian, C.S. Levin, *Phys. Med. Biol.* **61**, 7600 (2016).

[15] Y. Wang, L. Tao, S. Abbaszadeh, C. Levin, *Phys. Med. Biol.* **66**, 055013 (2021).